

RESEARCH ARTICLE OPEN ACCESS

Insights Into Improving the Li-Ion Transference Number and Li Deposition Uniformity Toward a High-Current-Density Lithium Metal Anode

Subi Yang^{1,2} | Seungho Lee^{1,2} | Min Sung Kang^{3,4} | Kwang Chul Roh²  | Jihoon Seo⁵ | Dongsoo Lee⁶ | Kwanghyun Kim^{1,2} | Sangkyu Lee⁷ | Sung Beom Cho^{3,4} | Patrick Joohyun Kim¹ | Junghyun Choi⁶ 

¹School of Chemical Engineering and Applied Chemistry, Kyungpook National University, Daehak-ro 80, Buk-gu, Daegu, Republic of Korea | ²Energy Storage Materials Center, Korea Institute of Ceramic Engineering and Technology, Jinju-si, Gyeongsangnam-do, Republic of Korea | ³Department of Materials Science and Engineering, Ajou University, Suwon, Gyeonggi-do, Republic of Korea | ⁴Department of Energy Systems Research, Ajou University, Suwon, Gyeonggi-do, Republic of Korea | ⁵Department of Chemical & Biomolecular Engineering, Clarkson University, Potsdam, New York, United States | ⁶School of Chemical, Biological and Battery Engineering, Gachon University, Seongnam-si, Gyeonggi-do, Republic of Korea | ⁷Department of Energy Science and Engineering, Kunsan National University, Gunsan-si, Jeonbuk-do, Republic of Korea

Correspondence: Sung Beom Cho (csb@ajou.ac.kr) | Patrick Joohyun Kim (pjkim@knu.ac.kr) | Junghyun Choi (junghchoi@gachon.ac.kr)

Received: 20 January 2025 | **Revised:** 28 April 2025 | **Accepted:** 26 May 2025

Funding: This study was supported by Ministry of Science and ICT, South Korea (RS-2024-00407282) and National Research Foundation of Korea (RS-2024-00408156).

Keywords: Li metal batteries | Li-ion conductivity | separator modification | uniform Li deposition

ABSTRACT

The practical application of lithium (Li) metal batteries (LMBs) faces challenges due to the irreversible Li deposition/dissolution process, which promotes Li dendrite growth with severe parasitic reactions during cycling. To address these issues, achieving uniform Li-ion flux and improving Li-ion conductivity of the separator are the top priorities. Herein, a separator (PCELS) with enhanced Li-ion conductivity, composed of polymer, ceramic, and electrically conductive carbon, is proposed to facilitate fast Li-ion transport kinetics and increase Li deposition uniformity of the LMBs. The PCELS immobilizes PF_6^- anions with high adsorption energies, leading to a high Li-ion transference number. Simultaneously, the PCELS shows excellent electrolyte wettability on both its sides, promoting rapid ion transport. Moreover, the electrically conductive carbon within the PCELS provides additional electron transport channels, enabling efficient charge transfer and uniform Li-ion flux. With these advantages, the PCELS achieves rapid Li-ion transport kinetics and uniform Li deposition, demonstrating excellent cycling stability over 100 cycles at a high current density of 12.0 mA cm^{-2} . Furthermore, the PCELS shows stable cycling performances in Li-S cell tests and delivers an excellent capacity retention of 95.45% in the Li|LiFePO₄ full-cell test with a high areal capacity of over 5.5 mAh cm^{-2} .

1 | Introduction

To mitigate rapid climate change and achieve net-zero emissions, the top priority is developing advanced batteries to replace traditional internal combustion engines with electric

vehicles (EVs) [1–3]. Consequently, the EV market has various requirements for rechargeable batteries, including high energy density, fast charging, and safety [4–7]. In this regard, lithium (Li)-ion batteries (LIBs) are the most widely used energy storage devices for EVs due to their excellent electrochemical

Subi Yang, Seungho Lee, and Min Sung Kang contributed equally to this study.

This is an open access article under the terms of the [Creative Commons Attribution](#) License, which permits use, distribution and reproduction in any medium, provided the original work is properly cited.

© 2025 The Author(s). *Carbon Energy* published by Wenzhou University and John Wiley & Sons Australia, Ltd.

performances [8–11]. However, as the conventional LIBs with graphite anodes cannot meet the ever-growing demands of the EV markets for higher energy densities, there is an urgent need to develop next-generation batteries [12–14]. As a potential alternative to conventional LIBs, Li metal batteries (LMBs) have attracted significant attention due to their very high theoretical specific capacity (3860 mAh g^{-1}) and low redox potential (-3.040 V vs. standard hydrogen electrode) of the Li metal anode [15–19]. However, several challenges hinder the practical implementation of LMBs, such as the formation of an unstable solid electrolyte interphase (SEI) layer, low Coulombic efficiency (CE), and dendritic Li growth during cycling [20–26]. Furthermore, uncontrollable Li dendrite growth during repetitive cycling can penetrate the separator, causing internal short-circuit and posing severe safety hazards [27–31].

To address these issues, an ideal separator design is required, which can play a role in suppressing Li dendrite growth, reducing safety concerns, and improving electrochemical performances of LMBs [32–35]. Polyolefin separators (polyethylene, polypropylene (PP), and their hybrids) are the most widely used separators in LMBs due to their superior chemical stability, uniform pore distribution, and low costs [36, 37]. However, the poor electrolyte wettability and low Li-ion transference number (t_{Li^+}) of polyolefin separators result in ununiform Li-ion flux, limiting their ability to support reversible electrochemical reactions and mitigate Li dendrite growth during cycling [38–42]. In addition, due to the poor mechanical strength and low thermal stability of polyolefin separators, they cannot withstand dendritic punctures and avoid short-circuits during cycling [43–47]. Therefore, improving the poor physicochemical properties of polyolefin separators through modification is crucial for achieving highly stable and high-performance LMBs.

In this study, a polymer–ceramic–electrically conductive carbon composite–layered separator (PCELS) is proposed to improve the Li-ion transport ability and uniformity of Li-ion flux. In addition to PCELS, a polymer–ceramic composite–layered separator (PCS) and polymer–electrically conductive carbon composite–layered separators (PES) were also systematically compared to elucidate the impact of specific structural and functional properties of separators on Li-ion transport kinetics, Li deposition behavior, and cycling stability in LMBs. Due to high affinity of the ceramic–polymer composite layer to PF_6^- anions in Li salts, the PCELS immobilizes the PF_6^- anions and facilitates selective Li-ion transport. Also, the high electrolyte wettability on both sides of the separator significantly improves the ionic conductivity [48]. Additionally, the electrically conductive carbon within the PCELS shortens the channels for ion transport by providing additional charge-transfer sites, promoting rapid electrochemical reactions [49–51]. Owing to these synergistic effects, the PCELS achieves uniform Li-ion flux and a reversible Li deposition/dissolution process during cycling. When the PCELS was evaluated in Li metal half-cell tests using conventional carbonate-based electrolytes without additives, the cell with the PCELS showed significantly improved cycle performances of an average CE of $\sim 96.5\%$ over 200 cycles at a current density of 4.0 mA cm^{-2} and stable cycling over 100 cycles even at a high current density of 12.0 mA cm^{-2} . Moreover, the PCELS delivered stable cycle performances in

Li-sulfur (S) cell, and $\text{Li}|\text{LiFePO}_4$ (LFP) full-cell tests with a high areal capacity of $\sim 5.5 \text{ mAh cm}^{-2}$. We believe that the proposed separator would pave the way for the design of LMB separators and further studies for practical implementation of LMBs.

2 | Experimental Section/Methods

2.1 | Preparation of the PCS, PES, and PCELS

The slurry for the PCS coating was prepared by mixing boehmite powder with 6 wt% polyvinylidene fluoride (PVDF) binder (at a 9:1 weight ratio). This mixture was then dispersed in N-methylpyrrolidone (NMP) using a planetary mixer (ARE-310, Thinky). The slurry for the PES coating was also prepared by mixing graphene powder with a poly(acrylic acid) (PAA) binder (at a 9:1 weight ratio). The slurries for PCS and PES coating were applied to the PP separator (Celgard 2400) with a doctor blade. The coated separators were then dried in a convection oven at 50°C for 12 h. The PCELS was prepared as follows: after the PCS was fully dried, the PES slurry was cast onto the opposite side of the polymer–ceramic coating layer. Subsequently, the PCELS was fully dried in the convection oven at 50°C for 12 h. Each separator was punched into a 19 mm diameter disk for cell assembly. The polymer–ceramic composite layer was coated at 1.14 mg cm^{-2} , and the polymer–electrically conductive carbon layer was coated at 0.60 mg cm^{-2} on each side of the PP separator.

2.2 | Electrode Preparation and Cell Assembly

The $\text{Li}|\text{Cu}$ cells were prepared using a 1 T Li metal foil (16 mm diameter) as the anode and a Cu foil (12 mm diameter) as the cathode. The electrolyte consisted of 1.0 M LiPF_6 dissolved in a mixture of ethylene carbonate (EC) and diethyl carbonate (DEC) (EC:DEC = 1:1, v/v) without any additives. The $\text{Li}|\text{Cu}$ coin cells (CR2032) were assembled in an argon-filled glovebox. To prepare the LFP electrode, a slurry was formulated by mixing LFP (LFP-NCO, Advanced Lithium Electrochemistry Co. Ltd.) as the active material, carbon black (Super P) as the conductive additive, and PVDF as the binder in NMP as the solvent. The slurry was uniformly coated onto a 20 μm -thick aluminum current collector and subsequently dried in a vacuum oven at 100°C overnight. The LFP electrode was then punched into 12 mm diameter disks at a loading level of $\sim 25 \text{ mg cm}^{-2}$. $\text{Li}|\text{LFP}$ full-cells were assembled with an electrolyte composed of 1.15 M LiPF_6 in a solvent mixture of EC, ethyl methyl carbonate (EMC) and DEC (EC:EMC:DEC = 2:4:4, v/v/v). The electrolyte was supplemented with 10 wt% fluoroethylene carbonate, 1 wt% LiPO_2F_2 , and 1 wt% vinylene carbonate (VC) as additives. The sulfur electrode slurry was prepared by mixing 60 wt% sulfur, 30 wt% Super P, and 10 wt % PVDF binder in an NMP solvent using a mixer. After mixing, the sulfur slurry was cast onto an aluminum foil and dried in a convection oven at 50°C for 24 h. After drying, the sulfur electrode was punched into a 12 mm diameter disk with a loading level of $\sim 1.5 \text{ mg cm}^{-2}$. The $\text{Li}|\text{S}$ coin cells were assembled in an argon-filled glovebox using an electrolyte of 1 M LiTFSI in a dimethoxy ethane/1,3-dioxolane (1:1, v/v) mixture with 2 wt% LiNO_3 .

2.3 | Characterization

The surfaces of PP, PCS, PES, and PCELS were analyzed using field emission scanning electron microscope (SEM, Hitachi SU8230). The chemical compositions of the PP, PCS, PES, and PCELS were analyzed using X-ray diffraction (XRD) on a diffractometer (D8 Advance, Bruker). The thermal shrinkage of each separator was determined by measuring the dimensional change before and after the thermal treatment at 100, 120, and 140°C for 1 h. Shrinkage was calculated using the following equation:

$$\text{Shrinkage } (\%) = \frac{S_0 - S_T}{S_0} \times 100\% \quad (1)$$

S_0 and S_T represent the areas of the separator before and after thermal treatment, respectively. The porosity of each separator was measured using a mercury porosimeter (Autopore V 9620, Micromeritics). The contact angle, indicating the wettability of the separators, was determined using a contact angle measurement (Phoenix 300, SEO).

2.4 | Electrochemical Measurement

The Li deposition/dissolution tests for Li|Cu cells were conducted with an areal capacity of 1.0 mAh cm⁻², and the cutoff voltage for Li dissolution was set to 1.0 V vs. Li⁺/Li. The cycling and rate performance tests for the Li|LFP cell were performed following a constant current-constant voltage protocol on a battery cycler (WBCS3000L32, WonATech). The ionic resistance of the electrolyte-wetted separator was measured using a potentiostat (VSP, Biologic, Seyssinet-Pariset) in stainless-steel (SUS)separatort-SUS symmetric cells over a frequency range from 300 kHz to 1 Hz with an AC amplitude of 10 mV. The internal resistance of each Li|Cu, Li-S, and Li|LFP cell after cycling was measured using electrochemical impedance spectroscopy (EIS) over a frequency range from 250 kHz to 10 mHz. Li|Li symmetric cells were assembled to measure the t_{Li^+} of each separator with an applied potential of 10 mV in the frequency range from 20 kHz to 1 Hz for 20,000 s. The t_{Li^+} of each separator was calculated using the following equation:

$$t_{Li^+} = \frac{I_{ss}(\Delta V - I_0 R_{p,0})}{I_0(\Delta V - I_{ss} R_{p,ss})} \quad (2)$$

where “ I_0 ” represents the initial current, “ I_{ss} ” denotes the steady-state current, “ ΔV ” indicates the applied potential, and “ $R_{p,0}$ ” and “ $R_{p,ss}$ ” are the resistances of the cells before and after polarization, respectively. The Li-S and Li|LFP cell tests were conducted at a current density of 0.5 C, with a voltage range of 1.7–2.8 V and 2.5–4.0 V, respectively.

The tortuosity (τ) of each separator was measured using the following equation:

$$\tau = \frac{R_{ohm} \times A \times K \times \varepsilon}{d} \quad (3)$$

where “ R_{ohm} ” is the ohmic resistance of the cell with each separator, “ A ” denotes the cross-sectional area, “ ε ” indicates

the porosity, “ d ” represents the thickness of each separator, and “ K ” is the conductivity of the electrolyte. The electrolyte capacities were evaluated by soaking each separator in 1.0 M LiPF₆ in EC:DEC (1:1, v/v) at room temperature for 12 h. After immersion, excess electrolyte on the surface of the separator was carefully removed using filter paper. The electrolyte capacities were then calculated using the following equation:

$$\text{Electrolyte capacity} = \frac{W - W_0}{S} \quad (4)$$

where “ W_0 ” and “ W ” are the weights of the separators before and after soaking in the electrolyte, respectively, and “ S ” indicates the surface areas of the separators.

The ionic conductivity (σ) of the separator was measured using the following equation:

$$\sigma = \frac{d}{R_{ion} \times S} \quad (5)$$

2.5 | Density Functional Theory (DFT) Calculation

DFT calculations were performed using the VASP package and projector-augmented wave potentials [52, 53]. The exchange-correlation potentials were defined using the generalized gradient approximation using Perdew–Burke–Ernzerhof [54]. The electronic wave functions were expanded in plane waves with a cutoff energy of 520 eV to minimize Pulay stress during structural optimization. Structural optimization was terminated when the Hellmann–Feynman forces reached the threshold value of 0.01 eV/Å. The Brillouin zone was sampled using (3×2×1), (2×2×2), and (1×1×1) k-point grids for boehmite (010), PP, and PAA, respectively. The interaction between the surface and adsorbates was described by adsorption energy (ΔE_{ads}) analysis, defined as

$$\Delta E_{ads} = E_{System} - (E_{Surface} + E_{adsorbate}) \quad (6)$$

where $E_{Surface}$ is the total energy of surfaces, $E_{adsorbate}$ denotes the total energy of the isolated atom, and E_{System} represents the total energy of the isolated atom adsorption system. A negative ΔE_{ads} value indicates an attractive interaction between the adsorbate and surfaces.

Finite element method (FEM) simulation: FEM simulation was used to investigate the Li behavior in the Li|Cu asymmetric cell. Li deposition modeling was performed using COMSOL Multiphysics 6.2 software. The model incorporates two types of physics, electrochemistry and ion transport, to simulate Li deposition behavior on the electrode during the charging process.

2.6 | Transportation of Species

The mass balance equations for each diluted species i in an electrolyte are described as follows:

$$\frac{\partial c_i}{\partial t} + \nabla \cdot J_i = 0 \quad (7)$$

where J_i is the flux of species i . The flux is described using the Nernst–Planck equations, which account for the diffusion, convection, and migration of the charged species. In this model, the transport of the charged ions through diffusion and migration was considered. Thus, the ionic flux is expressed as follows:

$$\mathbf{J}_i = -D_i \nabla c_i - \frac{D_i z_i F}{k_B T} c_i \nabla \phi_l \quad (8)$$

where D_i is the diffusion coefficient of i , c_i denotes the concentration of an ionic species i , z_i indicates the valence charge, F represents the Faraday constant, k_B denotes the Boltzmann constant, T is temperature, and ϕ_l is the electrolyte potential. The first and second terms on the right-hand side of the equation represent diffusion driven by the concentration gradient and electromigration influenced by the electric field, respectively.

2.7 | Electrochemistry

Electrochemical analysis was conducted using the secondary current distribution method, which accounts for concentration gradients and electrode kinetics. In this model, charge transport within the electrolyte was described using Ohm's law:

$$\mathbf{i}_l = -\sigma_l \nabla \phi_l \quad (9)$$

$$\nabla \cdot \mathbf{i}_l = 0 \quad (10)$$

where \mathbf{i}_l is the current density vector and σ_l denotes the electrical conductivity of the electrolyte. The lateral boundaries of geometry were defined to have null electric flux, ensuring periodic boundary conditions:

$$-\mathbf{n} \cdot \mathbf{i}_l = 0 \quad (11)$$

where \mathbf{n} is the normal vector to the boundary.

The current density at the electrode surface and overpotential were modeled using concentration-dependent kinetics, described using the Butler–Volmer equation:

$$i_{loc} = i_0 [c_R \exp\left(\frac{\alpha_a F \eta}{RT}\right) - c_O \exp\left(\frac{\alpha_c F \eta}{RT}\right)] \quad (12)$$

where i_{loc} indicates the local charge-transfer current density, i_0 represents the exchange current density, c_R and c_O are the concentrations of reduced and oxidized species, respectively, η is the overpotential, R denotes the gas constant, and α_a and α_c are the charge-transfer coefficients of the anode and the cathode, respectively. Supporting Information S1: Table S1 presents the specific parameters utilized in the modeling.

3 | Results and Discussion

Figure 1 illustrates how PCELS enhances the Li-ion transport ability and electrochemical performances of LMBs. The

ceramic–polymer composite layer shows excellent electrolyte wettability due to its porous structure. Additionally, the ceramic particles in the ceramic–polymer composite layer enhance t_{Li^+} through strong interactions with anions in the Li salts, promoting uniform Li deposition [32, 55, 56]. The electrically conductive carbon–polymer composite layer also shows high electrolyte wettability and increases t_{Li^+} due to the negatively charged functional groups in the polymer [57]. Furthermore, the electrically conductive carbon within the PCELS provides additional electron transport pathways, reducing local current densities applied to the counter electrode and facilitating uniform Li-ion flux [58, 59]. Consequently, the PCELS shows significantly improved Li-ion transport ability and uniformity of Li-ion flux. Owing to these synergistic effects, the PCELS shows excellent electrochemical performances and achieves uniform Li deposition/dissolution process, effectively mitigating Li dendrite growth during cycling.

Figure S1A,B illustrates the SEM images of the PCS and PES, respectively. For the PCS, ceramic particles are uniformly coated on the PP separator, with an average particle size of 200 nm, providing numerous sub-micron-sized pores (Supporting Information S1: Figure S1A). Supporting Information S1: Figure S1B depicts the homogeneous distribution of two-dimensional electrically conductive carbon on the PES, which retains its structural integrity after the coating process. The insets in Supporting Information S1: Figure S1A,B show photographic images of the coated sides of each separator, confirming that the coated sides of both separators are completely covered by each layer. To further verify the successful modification of the separators, XRD analysis was performed on each one (Supporting Information S1: Figure S1C). The XRD patterns of the PCELS show a strong peak at 26°, corresponding to electrically conductive carbon, along with additional peaks at 14°, 28°, 38°, and 48° and weak peaks at 13°, 17°, and 19° due to ceramic particles and the PP separator, respectively [60, 61]. These findings indicate that both sides of the PCELS are successfully modified by the respective coating layers. Additionally, the cross-sectional SEM images prove the uniformity of each coating layer. Supporting Information S1: Figure S1D–F illustrates the cross-sectional SEM images of the PCS, PES, and PCELS, respectively. The SEM images illustrate that the ceramic–polymer and electrically conductive carbon–polymer composite layers are coated at 10 and 20 μm thickness, respectively, with uniform and robust adhesion at each side of the separator.

The thermal stability of the separator at high temperatures is a crucial factor influencing battery safety. An internal short-circuit caused by Li dendrite growth is accompanied by abnormal heat generation. This phenomenon causes thermal shrinkage of the separator, thereby increasing the contact area between the cathode and the anode. The increased contact area then accelerates Joule heating, resulting in thermal runaway and a potential risk of fire and explosion of the batteries [62–64]. Hence, separators with high thermal stability and mechanical strength are essential for mitigating the risks mentioned above. To evaluate the thermal stability of each separator, thermal shrinkage measurements were conducted at 100°C, 120°C, and 140°C for 1 h (Supporting Information S1: Figure S2A). The PP showed shrinkage at 120°C, with a

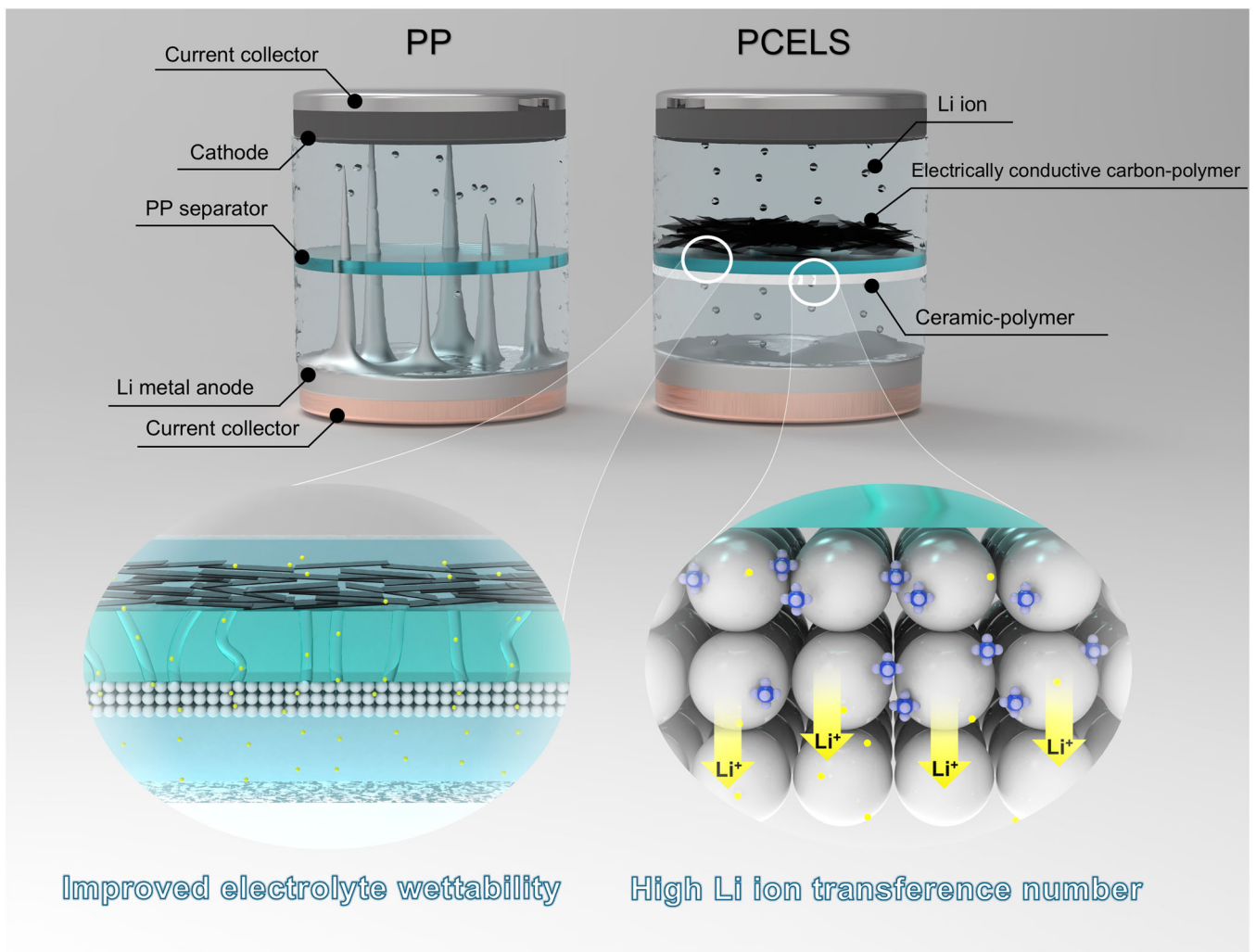


FIGURE 1 | Schematic image illustrating the effects of PCELS on Li-ion transport kinetics and Li deposition behavior.

significant reduction of 28% at 140°C. In contrast, the PCS and PES showed enhanced thermal stability, with thermal shrinkages of 18% and 9%, respectively, at 140°C. In addition, the PCELS demonstrated outstanding thermal stability, with a less than 1% reduction in its original area even after being exposed to a temperature of 140°C for 1 h. This enhanced thermal stability may be attributed to the incorporation of both coating layers, which offer high thermal resistance and provide mechanical strength to endure physical shrinkage of the separator. The uniformly distributed ceramic particles and carbon with high thermal conductivity prevent localized heat accumulation and enhance the overall thermal stability of the separator [65]. Additionally, the polymers on both sides of PCELS further enhance its thermal stability and mechanical strength, enabling prevention of thermal shrinkage. Consequently, the PCELS effectively mitigates thermal shrinkage at elevated temperatures (Supporting Information S1: Figure S2B).

To investigate the effects of ceramic particles on the Li-ion transport kinetics, DFT calculations were performed to evaluate the adsorption energies of PF_6^- and Li^+ on the PP and ceramic particles (Figure 2A). The PF_6^- adsorption energies were calculated to be -1.77 and -4.16 eV on the PP and ceramic particles, respectively. These negative adsorption energy values

indicate attractive interactions between the ions and surfaces, with larger magnitudes corresponding to stronger binding. The substantially more negative adsorption energy on the ceramic particles indicates enhanced anion interactions, suggesting that integrating ceramic particles onto the separator significantly improves anion adsorption compared to that of the PP [66]. This increased anion interaction subsequently facilitates selective Li-ion transport. Additionally, Li adsorption energies of -0.08 eV on PP and -0.98 eV on ceramic particles indicate that ceramic particles improve Li interactions, promoting dissolution of Li ions and thereby contributing to superior transport properties. These findings suggest that the ceramic–polymer composite layer enhances anion adsorption and modulates Li-ion interactions, supporting more efficient Li-ion transport. In addition to ceramic particles, the PAA used as a polymer for the PES surface also aids in dissolving the Li ions and enhancing their transport ability. Hao et al. reported that the PAA chains within the separator provide abundant $-\text{COO}^-$ groups, which facilitate the movement of Li ions while mitigating the free migration of PF_6^- anions [57]. This mechanism promotes Li-ion dissolution and fast Li-ion transport, enabling uniform Li deposition. In addition, Lin et al. also reported that incorporating $-\text{COOH}$ groups into the separators significantly enhances Li-ion transport ability [67]. These findings suggest that the electrically

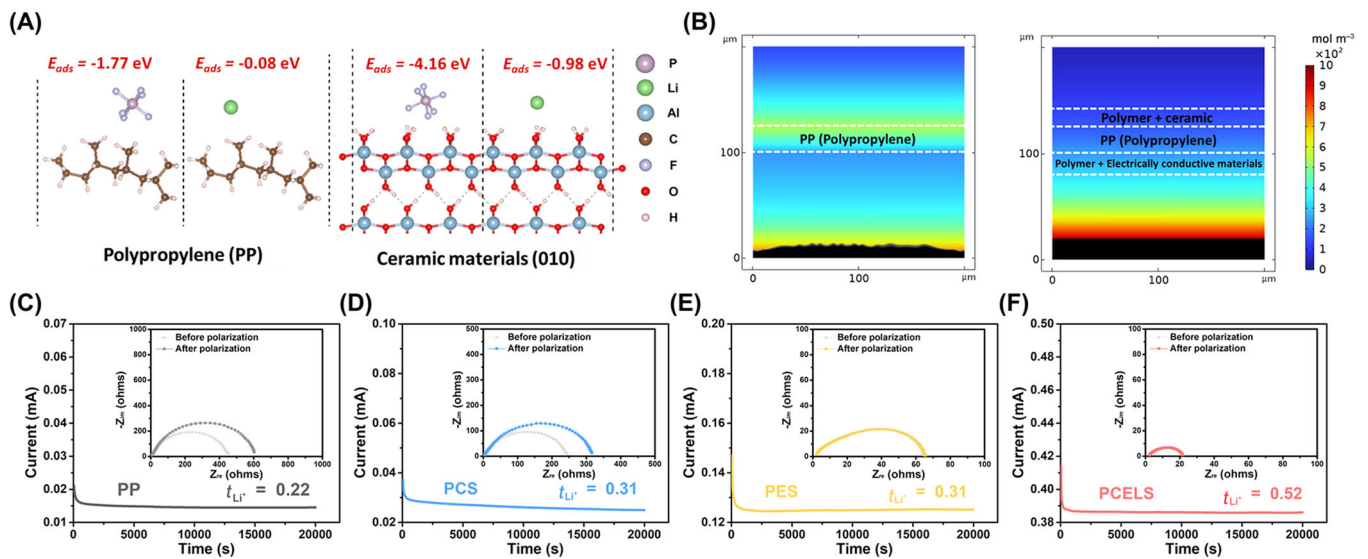


FIGURE 2 | (A) Comparison of PF_6^- and Li^+ adsorption energies on PP and ceramic particles. (B) Distribution of the Li concentration and simulated dendrite growth morphology for PP and PCELS, respectively. EIS spectra before and after the polarization test, along with the corresponding polarization curves for (C) PP, (D) PCS, (E) PES, and (F) PCELS evaluated in a $\text{Li}|\text{Li}$ symmetric cell for t_{Li^+} measurement.

conductive carbon–polymer composite layer also improves Li-ion transfer kinetics, and thus, the PCELS may significantly enhance selective Li-ion transport ability.

To investigate the Li deposition behavior for PP and PCELS, FEM simulations were conducted using COMSOL Multiphysics. The Li diffusivity value of the PP was determined using the Langmuir isotherm model, which describes adsorption kinetics as follows:

$$k_a \propto \exp\left(-\frac{E_{ads}}{RT}\right) \quad (13)$$

where k_a denotes the adsorption constant for the system, R indicates the gas constant, and E_{ads} represents the adsorption energy obtained from DFT calculations. Using the Li-ion diffusion coefficient (D_{Li^+}) of PES in Figure 4I as a reference value ($4.175 \times 10^{-10} \text{ cm}^2 \text{ s}^{-1}$), we derived D_{Li^+} of the PP separator based on the adsorption energy ratio obtained from the DFT calculations. The resulting D_{Li^+} for the PP was $1.712 \times 10^{-10} \text{ cm}^2 \text{ s}^{-1}$. Figure 2B illustrates the simulated Li deposition morphologies for both PP and PCELS. The results showed that the PCELS promotes the uniform distribution of Li ions and even Li deposition due to its enhanced Li-ion transport ability. In contrast, the PP, with its limited Li-ion transport ability, shows the accumulation of Li ions on its surface and uneven Li-ion flux, leading to dendritic Li growth. These findings indicate that the PCELS effectively improves the Li-ion transfer kinetics, promoting uniform Li deposition.

To further investigate the effect of each coating layer on Li-ion transport, $\text{Li}|\text{Li}$ symmetric cells were assembled with each separator to measure the t_{Li^+} . The increase in t_{Li^+} promoted uniform Li deposition and suppressed dendritic Li formation during the charging process, as proposed in Chazalvie's electromigration limited model [68]. According to Chazalvie's model based on Sand's time, a high anion transference number

accelerates the formation of an “ion depletion layer,” which promotes dendritic Li growth [69]. Sand's time (t_{Sand}), defined as the time required for dendritic Li formation, is expressed as follows:

$$t_{\text{Sand}} = \pi D \left(\frac{eC_0}{2J(1 - t_{\text{Li}^+})} \right)^2 \quad (14)$$

In the equation, t_{Sand} is inversely proportional to $(1 - t_{\text{Li}^+})^2$, indicating that a higher t_{Li^+} value leads to an increase in t_{Sand} , which indicates the mitigation of Li dendrite growth. The t_{Li^+} value of the cells was measured using the Bruce–Vincent method [70]. The t_{Li^+} values for the PP and PCS were 0.22 and 0.31, respectively. This difference is attributed to the strong binding force of the ceramic particles with PF_6^- anions in the Li salts, as shown in the DFT results (Figure 2C,D). For the PES, the t_{Li^+} value also increased to 0.31 due to the negatively charged carboxyl groups of the PAA, which interact with solvated Li ions and improve the transport ability of the Li ions (Figure 2E). With the synergistic effects of both coating layers, the PCELS showed a significantly improved t_{Li^+} value of 0.52, considerably mitigating dendritic Li nucleation, as demonstrated by the FEM simulation results (Figure 2F).

The electrolyte wettability of the separator plays a crucial role in improving the electrochemical performances of LMBs by enhancing ionic conductivity and promoting uniform Li-ion flux [71]. Given this, contact angle measurements were conducted for PP and each coating layer (Figure 3A–C). The PP separator showed a high contact angle of 102° , indicating poor electrolyte wettability (Figure 3A). In contrast, the electrolyte wettability of the coated separators was significantly improved, with contact angles of 33° and 54° for PCS and PES, respectively. These enhancements are attributed to abundant functional groups within the coating layers, along with their porous structures. This implies that the PCELS shows high electrolyte affinity on both sides of the separator, facilitating rapid ion transport

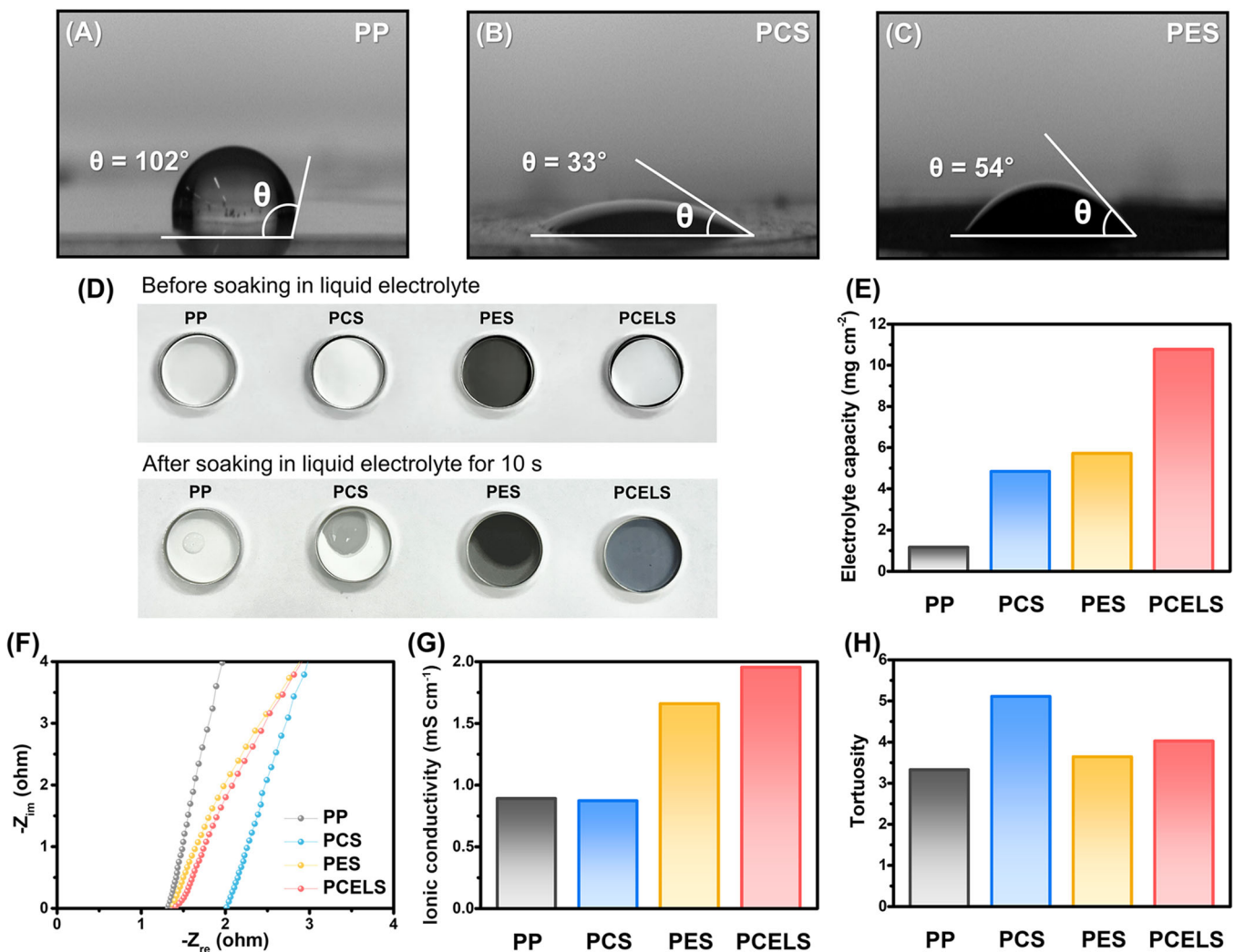


FIGURE 3 | Polar solvent contact angle measurements of (A) PP, (B) PCS, and (C) PES. (D) Photographic images of each separator before and after electrolyte uptake tests (before and 10 s after electrolyte drop). (E) Maximum electrolyte storage capacity of each separator. (F) Ionic conductivity tests for each separator in the SUSISUS cell and (G) summary of the ionic conductivity results. (H) Tortuosity of each separator calculated using the EIS method.

during cycling. In addition to the electrolyte wettability, an ideal separator for LMBs should efficiently absorb the electrolyte and reach saturation within 60 s [63, 72, 73]. Therefore, electrolyte uptake tests were conducted, serving as a critical indicator for evaluating the speed at which a separator absorbs the electrolyte and reaches saturation. The PP showed the lowest electrolyte uptake ability among the investigated separators (Figure 3D). In contrast, the PES and PCS absorbed more electrolytes than the PP due to the additional coating layers with abundant hydrophilic functional groups and high porosity. Moreover, the PCELS rapidly absorbed the electrolyte across its entire surface within 10 s after applying a single drop. These findings demonstrate the superior electrolyte uptake ability of the PCELS.

The maximum electrolyte storage capacity of each separator was also measured by immersing them in an electrolyte for 12 h (Figure 3E). The electrolyte capacity results showed that the PCELS had a substantial electrolyte capacity of approximately $10.765 \text{ mg cm}^{-2}$, compared to that of 5.705 mg cm^{-2} for PES, 4.824 mg cm^{-2} for PCS, and 1.147 mg cm^{-2} for PP. The

differences in electrolyte storage capacity among the separators are attributed to their respective pore structures and surface properties. The PP, with its low porosity and hydrophobic properties, shows a limited electrolyte storage capacity. In contrast, the PCS rich in hydroxyl groups shows enhanced electrolyte interactions and increased hydrophilicity. Additionally, the PCS provides abundant porous structures, further enhancing electrolyte storage capacity (Supporting Information S1: Figure S3). The PES also has high porosity compared to the PP, and the carboxyl groups of the PAA in the PES form strong bonds with the electrolyte, thereby maximizing electrolyte uptake. This property facilitates a more uniform distribution of the electrolyte, significantly enhancing the electrolyte storage capacity. Owing to the synergistic effects of both coating layers, the PCELS showed significantly improved electrolyte uptake and storage capacity, making it highly advantageous as a separator in liquid-electrolyte-based LMBs.

To investigate the effect of enhanced electrolyte wettability on the ionic conductivity of the separator—another key indicator in evaluating LMBs—EIS spectra were obtained for

SUS|separator|SUS symmetric cells using each separator (Figure 3F). The ionic conductivity values were 0.888, 0.870, 1.658, and 1.954 mS cm⁻¹ for the PP, PCS, PES, and PCELS, respectively (Figure 3G). Despite the significantly enhanced electrolyte wettability, the PCS showed nearly same ionic conductivity as the PP. However, the PES showed a higher ionic conductivity than the PP, likely due to the enhanced electrolyte wettability, which facilitates seamless electrolyte permeation within the separator. Moreover, the PCELS showed an even higher ionic conductivity of 1.954 mS cm⁻¹, which is two times higher than that of the PP. To clarify the reason for the ionic conductivity result, the tortuosity of each separator was measured (Figure 3H). As shown in Figure 3H, the PCS showed a significantly higher tortuosity (5.10) than the PP separator (3.19) due to the ceramic particles coated on the surface, which increase the ion transport pathways. These extended ion pathways hinder rapid ion transport within the separator, leading to poor ionic conductivity despite the improved electrolyte wettability. In contrast, the PES showed a slight increase in tortuosity (3.63) compared to the PP separator despite the additional coating layer. This is attributed to the high electrical conductivity of the PES, which provides additional electron transport channels that offset the extended ion transport pathway caused by additional coating. Moreover, the enhanced electrolyte wettability of the PES facilitated fast ion transport, resulting in significantly improved ionic conductivity compared to that of the PP. Similarly, the PCELS showed a significantly lower tortuosity value (4.02) than the PCS due to the enhanced electrical conductivity, which reduces the overall tortuosity of the separator by providing multiple charge-transfer sites. Given these findings, the significantly enhanced ionic conductivity of the PCELS may be attributed to the synergistic effects of both coating layers. With its high electrical conductivity, the PCELS shortens the ion transport pathways, whereas both coating layers considerably enhance the electrolyte wettability on both sides of the separator, leading to extensively enhanced ionic conductivity.

Galvanostatic charge–discharge tests were conducted to assess the effect of PCELS on the electrochemical reversibility of the Li deposition/dissolution process. Li|Cu cells incorporating PP, PCS, PES, and PCELS (i.e., PP, PCS, PES, and PCELS cells, respectively) were tested at current densities of 4 and 12 mA cm⁻². At a current density of 4 mA cm⁻², the PP cell showed a sharp decline in CE after 30 cycles, attributed to its poor ionic conductivity and low t_{Li^+} , which caused uneven Li deposition/dissolution and the formation of Li dendrites (Figure 4A). In the PCS cell, a similar tendency in CE was also observed during cycling, indicating that the PCS does not effectively mitigate the problems of irreversible Li deposition/dissolution, which is due to its poor ionic conductivity and high tortuosity. This was further evidenced by the initial voltage profiles of the PP and PCS cells (Figure 4B,C). The PCS cell showed higher voltage hysteresis (289 mV) compared to that of the PP cell (173 mV) during the initial cycle, indicating increased Li-ion transport impedance due to its high tortuosity. Despite the high resistance of PCS, the PCS cell showed similar cycle performance compared to that of the PP cell due to the enhanced wettability and increased t_{Li^+} . In contrast, the PES cell maintained a CE above 80% for up to 150 cycles due to the high electrical conductivity, which provides additional electron pathways and reduces the local current densities applied to the counter electrode, promoting uniform

Li-ion flux. Furthermore, the PES enhanced the t_{Li^+} and electrolyte wettability of the separator, leading to high ionic conductivity. However, the CE of the PES cell rapidly decreased after 150 cycles due to the growth of Li dendrites and the formation of dead Li during repeated cycling. Similarly, the voltage hysteresis of the PES cell increased from 196 to 226 mV after 100 cycles, indirectly indicating irreversible electrochemical reactions during cycling (Figure 4D). Meanwhile, the PCELS cell showed the best cycle stability among the evaluated cells, maintaining an average CE of 96.5% up to 200 cycles without a noticeable degradation. Additionally, the PCELS showed the lowest voltage hysteresis of 169 mV during the initial cycle, with only a slight increase to 172 mV after 100 cycles, indicating reversible electrochemical reactions during cycling (Figure 4E). In the case of PES and PCELS, the voltage profiles show a voltage hump above 0 V during the Li plating/stripping process, which is not observed in those using separators without a carbon coating layer. This phenomenon is attributed to the occurrence of a mild lithiation reaction at the carbon surface. Furthermore, the PCELS still shows the lithiation region even after 100 cycles, reflecting its excellent electrochemical reversibility [49]. The superior performance of the PCELS cell is attributed to the combined effects of both coating layers. The PCELS significantly increased t_{Li^+} , promoting a uniform Li deposition/dissolution process. Also, the enhanced electrolyte wettability on both sides of the separator ensured seamless electrolyte distribution, promoting rapid ion transport and uniform Li-ion flux. Additionally, the PCELS with high electrical conductivity further promotes uniform Li-ion flux, resulting in excellent cycling stability. These advantages become more evident in the cycle performance at a higher current density. Similar to the performance at a lower current density, both PP and PCS cells showed a sharp decline in CE after 25 cycles at 12.0 mA cm⁻² (Supporting Information S1: Figure S4A). The PCS cell also showed significantly higher voltage hysteresis of 565 mV compared to that of 425 mV for the PP cell, similar to the results at 4.0 mA cm⁻² (Supporting Information S1: Figure S4B,C). The PES cell demonstrated better cycle stability than the PP and PCS cells due to its high ionic conductivity (Supporting Information S1: Figure S4D). Furthermore, the PCELS cell maintained stable cycling performance over 100 cycles at a high current density of 12.0 mA cm⁻², with smaller voltage hysteresis of 375 mV than the PES cell (386 mV) (Supporting Information S1: Figure S4E). These results are attributed to the synergistically enhanced Li-ion transport ability, further demonstrating the advantages of the PCELS.

To evaluate the enhanced Li-ion transport ability of the PCELS, galvanostatic intermittent titration technique (GITT) tests were performed, which is an effective method for determining the D_{Li^+} . Owing to the absence of porous structures capable of conducting electrons and storing Li ions, the GITT tests could not be performed on the Li|Cu cell with the PP and PCS. Therefore, GITT tests were conducted on the PES and PCELS cells (Figure 4F,G) [74, 75]. Figure 4H depicts the specific IR drop values for the PES and PCELS, derived from the GITT curves. The PCELS cell showed smaller IR drop values than the PES cell overall, attributed to its higher ionic conductivity and increased t_{Li^+} (Figure 4H). The D_{Li^+} of each separator was determined

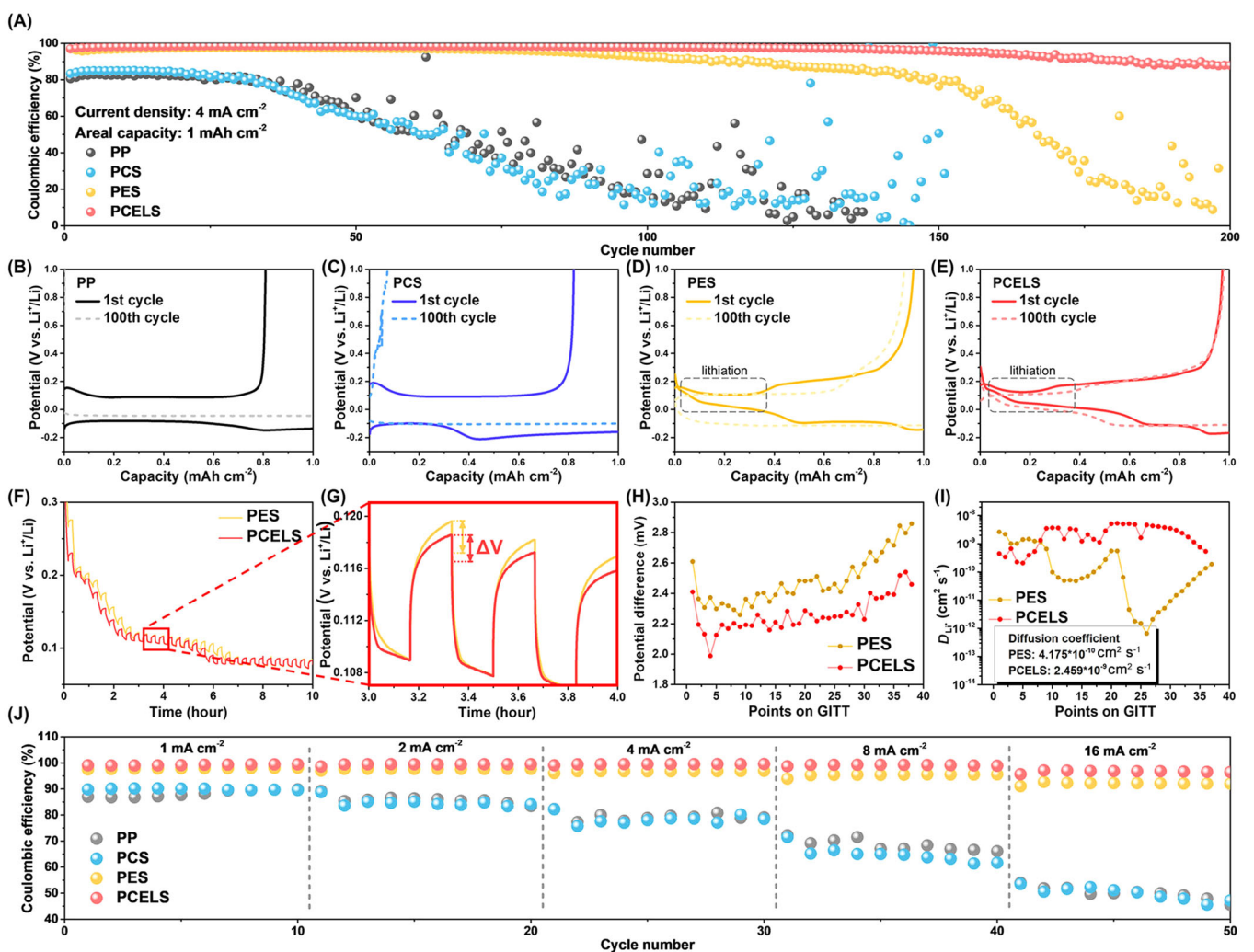


FIGURE 4 | (A) Cycle performance of Li metal half-cells with each separator at a current density of 4.0 mA cm^{-2} with an areal capacity of 1.0 mAh cm^{-2} . Voltage profiles at the initial cycle and the 100th cycle of the (B) PP, (C) PCS, (D) PES, and (E) PCELS cells. (F) GITT curves for the PES and PCELS cells and (G) enlarged part of the red-boxed regions. (H) Specific IR drop values of each cell based on the GITT curves and (I) corresponding D_{Li^+} calculated using Fick's 2nd law. (J) Rate performance of each Li metal cell at various current densities ranging from 1.0 mA cm^{-2} to 16.0 mA cm^{-2} .

from the IR drop values using the following equation (Fick's 2nd law):

$$D_{\text{Li}^+} = \frac{4}{\pi \tau} \left(\frac{m_B}{\rho S} \right)^2 \left(\frac{\Delta E_s}{\Delta E_t} \right)^2 \quad (15)$$

where τ denotes the duration of the titration step, S indicates the area of the coated separator, m_B represents the mass of the coating layer, and ρ is the density of the electrically conductive carbon. ΔE_t and ΔE_s represent the voltage changes during the titration and relaxation steps, respectively [76]. The PCELS cell showed an average D_{Li^+} value of $2.459 \times 10^{-9} \text{ cm}^2 \text{ s}^{-1}$, which is approximately five times higher than the value of the PES cell ($4.175 \times 10^{-10} \text{ cm}^2 \text{ s}^{-1}$) and over 14 times higher than the D_{Li^+} value of the PP cell ($1.712 \times 10^{-10} \text{ cm}^2 \text{ s}^{-1}$), as determined using the FEM simulation (Figure 4I). This result is attributed to the high t_{Li^+} and enhanced ionic conductivity of the PCELS, which synergistically improved Li-ion conductivity. To increase the validity of the GITT results, rate performance tests were performed (Figure 4J and Supporting Information S1: Figure S5).

The CE of the PP and PCS cells significantly decreased with increasing current density, attributed to the low ionic conductivity of the separators. The PES cell maintained significantly higher CEs than the PP and PCS cells at high current densities, further demonstrating its excellent electrical and ionic conductivity. Moreover, the PCELS cell also showed superior rate performances compared to that of the PES cell due to its high Li-ion transport ability, further confirming the GITT results.

EIS analyses were conducted during cycling to investigate the effect of each coating layer on cell resistance (Supporting Information S1: Figure S6). The values of cell resistance (SEI resistance (R_{SEI}) + charge-transfer resistance (R_{ct}), semicircle in the low- and middle-frequency range) at distinct cycles are summarized in Figure 5A-D. After the initial cycle, the PCS cell showed higher resistance than the PP cell despite the improved electrolyte wettability. This is attributed to the insulating coating layer with high tortuosity, which acts as a resistive layer during cycling. In contrast, the PES and PCELS cells showed significantly lower cell resistance than the PP cell due to the

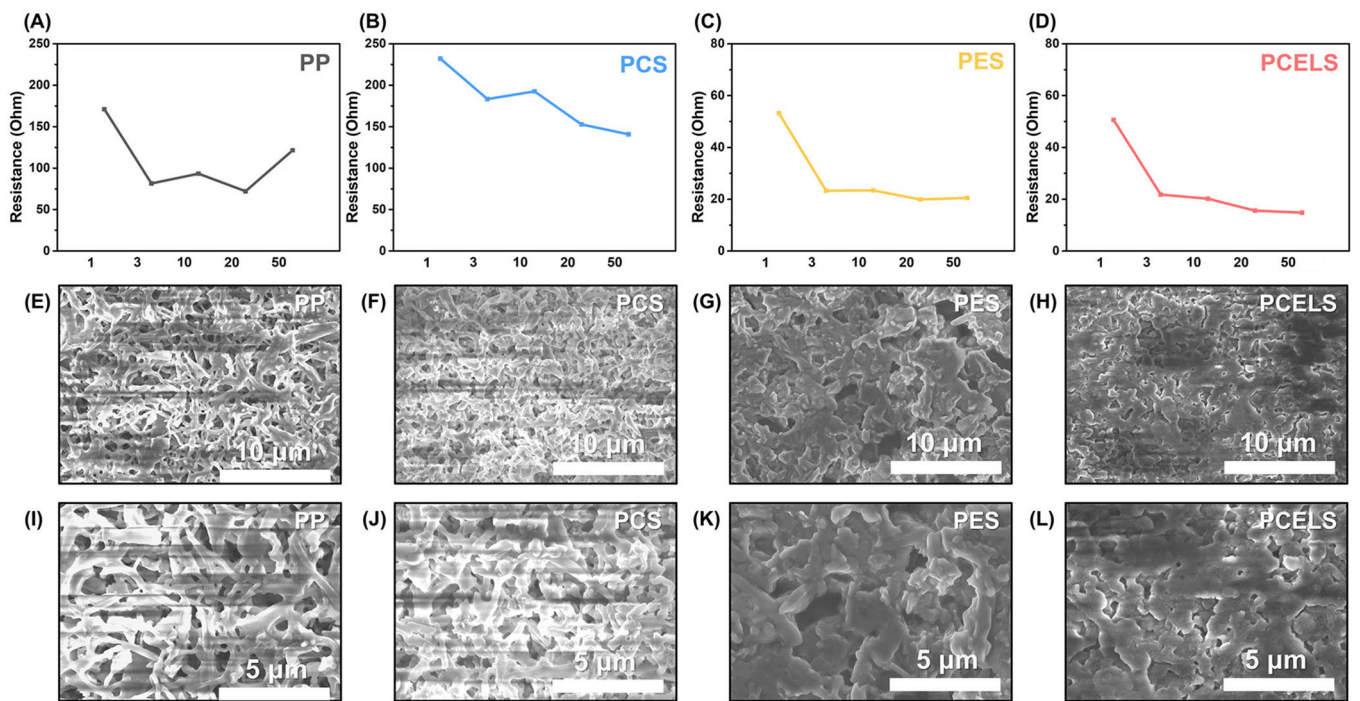


FIGURE 5 | EIS spectra of the (A) PP, (B) PCS, (C) PES, and (D) PCELS cells at different cycles. Post-mortem SEM and enlarged images of the Li deposits on Cu in the (E, I) PP, (F, J) PCS, (G, K) PES, and (H, L) PCELS cells, respectively.

excellent electrical conductivity. The electrically conductive carbon on the separator provides additional channels for electron transfer, thereby reducing the R_{ct} [77]. As the cycle progresses, the PP cell still shows high cell resistances of about $100\ \Omega$, which indicates irreversible electrochemical reactions. Additionally, the Warburg impedance (Z_w , slope of the linear part in the low-frequency range) related to the ionic transport resistance deteriorates with cycling, reflecting the sluggish ionic conductivity of the PP (Supporting Information S1: Figure S6A) [78]. The PCS cell showed a similar trend in the cell resistance and Z_w , indicating the poor ionic conductivity due to the high tortuosity and the resulting Li dendrite growth. In contrast, the PES cell maintained a significantly lower and constant cell resistance compared to those of the PP and PCS cell, suggesting uniform Li deposition during cycling. Additionally, the PES cell retained its Z_w during cycling due to the excellent electrical conductivity, consistent with the ionic conductivity results. Furthermore, the PCELS cell showed an even lower resistance than the PES cell after 20 cycles despite the presence of an additional insulating layer, which is attributed to the synergistically enhanced Li-ion conductivity that promotes rapid charge transfer.

To examine the Li deposition morphologies in cells with each separator, post-mortem studies were conducted after 100 cycles at a current density of 4 mA cm^{-2} . Figure 5E,I depicts the top-view SEM images of the Cu with the PP, confirming severe dendritic Li growth, which is attributed to the low t_{Li^+} and poor Li-ion conductivity. Similarly, severe dendritic Li growth was observed when the PCS was used (Figure 5F,J). Despite enhanced electrolyte wettability and t_{Li^+} , the high tortuosity of the PCS increased cell resistance, caused uneven Li-ion flux, and led to dendritic Li growth, which is consistent with the EIS results. In contrast, when PES was used, mossy Li deposits were

observed, attributed to the improved t_{Li^+} and high Li-ion conductivity (Figure 5G,K). In addition, the electrically conductive carbon within the PES acts as a lithiophilic matrix, promoting uniform Li-ion flux during cycling and facilitating the reversible Li deposition/dissolution process. In the cell with PCELS, almost no Li dendrites were observed, except for flat and smooth Li morphologies (Figure 5H,L). This result is attributed to the synergistic effects of the aforementioned advantages of the PES, significantly increased t_{Li^+} , and high electrolyte wettability on both sides, which enhance the uniformity of Li-ion flux and mitigate dendritic Li growth.

To evaluate the electrochemical performance of the PCELS under practical conditions, Li-S full-cell tests were conducted within a voltage window of $1.7\text{--}2.8\text{ V}$ at a current density of 0.5 C . Figure 6A depicts the cycling performance of Li-S cells using the PP and PCELS. The Li-S cell with the PP delivered a low initial capacity of 732.5 mAh g^{-1} and rapid capacity decay during the initial few cycles, attributed to incomplete electrode activation. In contrast, the Li-S cell with the PCELS showed a significantly higher initial capacity of 927.1 mAh g^{-1} , with no rapid capacity degradation. This improvement is attributed to the high electrical conductivity of the PCELS, providing additional electron transport channels and reactivating inactive sulfur [79]. Additionally, the Li-S cell with the PCELS showed a higher capacity retention of 61.9% after 200 cycles than the cell with the PP (42.6%), also retaining a high average CE of 97.5% over 200 cycles. These favorable results are attributed to the high Li-ion conductivity and increased t_{Li^+} , which mitigate the degradation of the Li metal anode and reduce irreversible electrochemical reactions during cycling.

Figure 6B,C illustrates the voltage profiles of each cell during the initial and final cycles. These profiles confirm that the Li-S

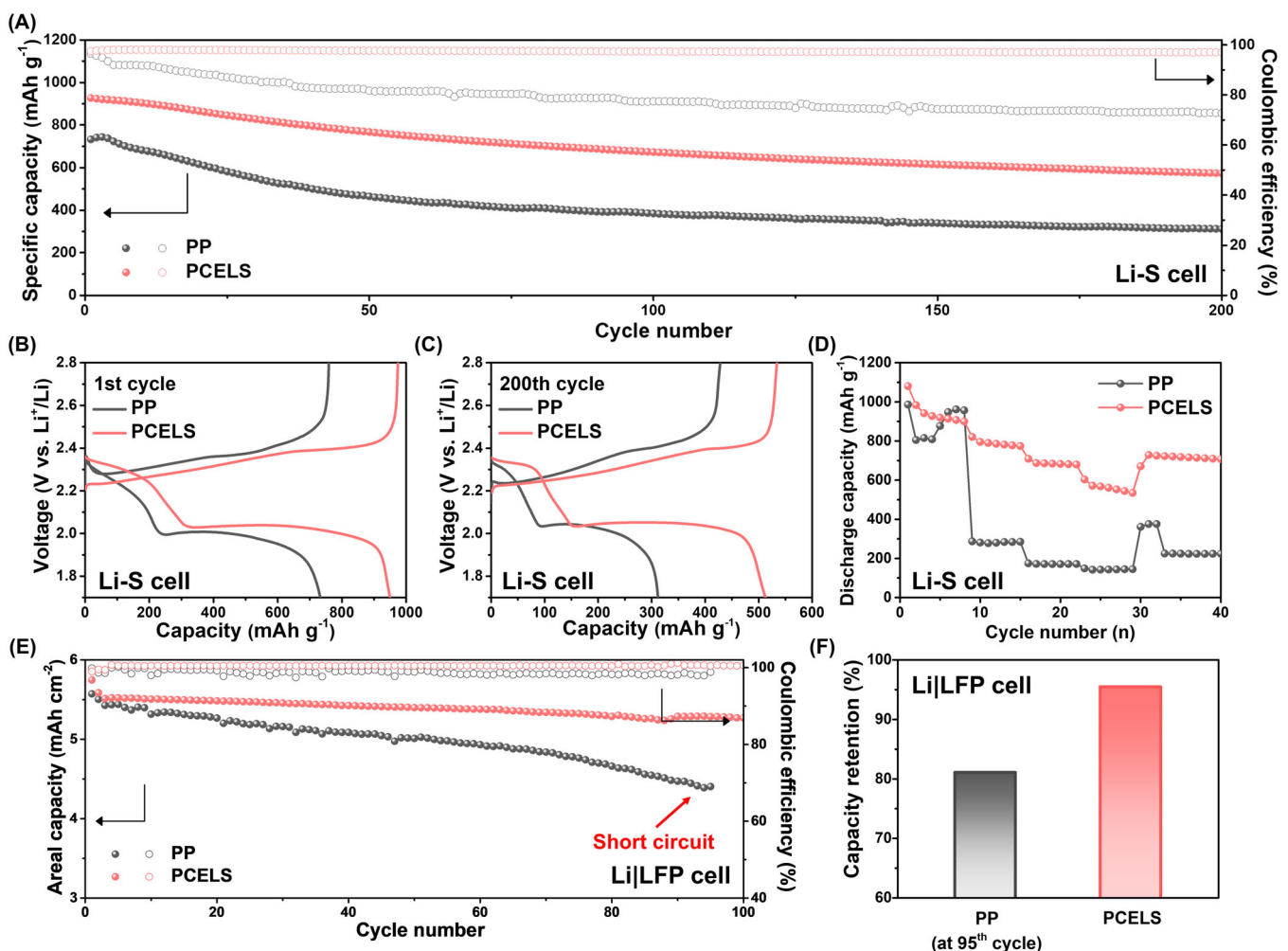


FIGURE 6 | (A) Cycle performance of Li-S cells with PP and PCELS. Voltage profiles of each cell in the (B) initial cycle and (C) final cycle. (D) Rate capability tests for each Li-S cell at various current densities ranging from 0.2 to 2 C. (E) Cycle performances and (F) capacity retention of Li|LFP cells with PP and PCELS.

cell with the PCELS showed smaller voltage hysteresis than the cell with the PP in both cases, indicating reduced cell resistance. To further investigate cell resistance, EIS tests were conducted. After the initial cycle, the Li-S cell with the PCELS showed similar cell resistance to that with the PP (Supporting Information S1: Figure S7A). However, after 200 cycles, the Li-S cell with the PCELS showed a significantly lower R_{ct} than the cell with the PP, indicating reversible electrochemical reactions and uniform Li deposition during cycling, effectively reducing cell resistance (Supporting Information S1: Figure S7B). Furthermore, rate capability tests were performed at various current densities ranging from 0.2 to 3 C (Figure 6D). The Li-S cell with the PP showed unstable cycling stability at 0.2 C and showed a significant capacity drop as the current density increased to 0.5 C. In contrast, the Li-S cell with the PCELS demonstrated excellent cycling stability, even at high current densities. Moreover, when the current density was reduced to 0.5 C, the Li-S cell with the PP showed a low capacity of 225 mAh g⁻¹, whereas the cell with the PCELS showed a high capacity of 728 mAh g⁻¹. This further highlights the high Li-ion conductivity and rapid Li-ion kinetics of the PCELS, which mitigate the degradation of the Li metal anode and improve the electrochemical performances of the Li-S cells.

To further evaluate the practical feasibility of the PCELS in LMBs, Li|LFP full-cells incorporating the PP and PCELS were assembled with an LFP cathode with a high areal capacity of over 5.5 mAh cm⁻². Figure 6E shows the cycling performance of the Li|LFP cells equipped with each separator. The Li|LFP cell incorporating the PP showed unstable cycling performances of fluctuating CEs with a low average CE of ~98.7%, accompanied by short-circuit at the 96th cycle (Supporting Information S1: Figure S8). In contrast, the Li|LFP cell with the PCELS delivered excellent cycling stability over 100 cycles, with a high average CE of over 99.7%. Also, the Li|LFP cell with the PCELS achieved excellent capacity retention of 95.5% after 100 cycles compared to the cell with the PP (81.0% at the 95th cycle) (Figure 6F). Moreover, the Li|LFP cell with the PCELS showed smaller cell resistance than the cell with the PP after the first cycle and showed similar resistance values after 100 cycles (Supporting Information S1: Figure S9). These results further demonstrate that the PCELS effectively improves the electrochemical reversibility of the LMBs owing to the excellent Li-ion transport ability, which is in good agreement with the Li metal half-cell and Li-S full-cell data.

The beneficial effects of the PCELS in improving the Li-ion transfer kinetics and Li deposition uniformity of the LMBs are

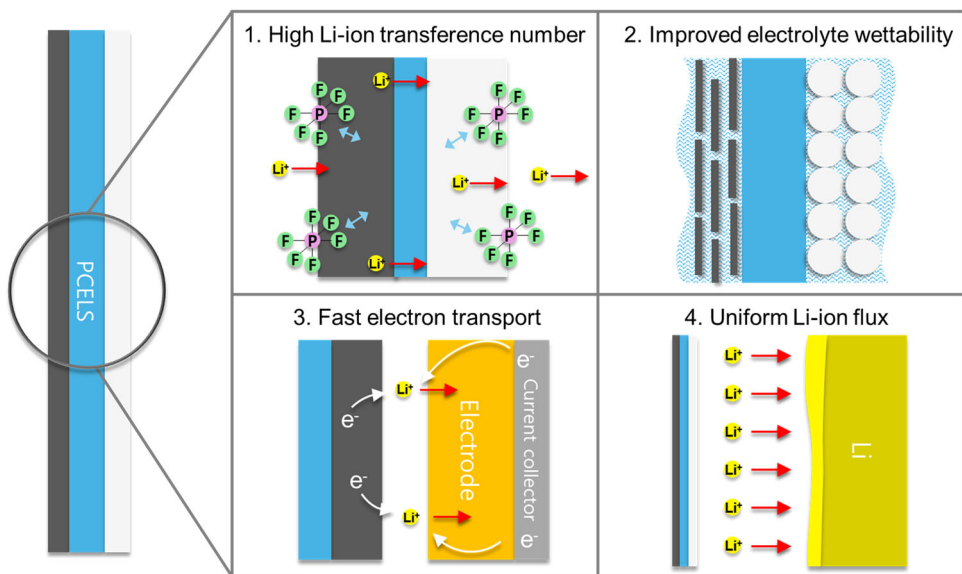


FIGURE 7 | Summarized scheme of the beneficial effects of PCELS on Li-ion transfer kinetics and electrochemical performances of LMBs.

summarized in Figure 7. The ceramic particles and negatively charged polymer strongly immobilize the PF_6^- anions, improving the t_{Li^+} . The high t_{Li^+} contributes to an increase in t_{sand} , implying the mitigation of Li dendrite growth. Also, the high electrolyte wettability on both sides of the PCELS leads to seamless ion transport within the separator, enhancing the ionic conductivity. Due to the high t_{Li^+} and ionic conductivity, the PCELS shows significantly improved Li-ion conductivity. Moreover, the PCELS with high electrical conductivity provides additional electron transport pathways to the electrode. This facilitates rapid charge transfer and efficient reactions, further enhancing the Li-ion conductivity. Owing to these benefits, the PCELS achieves uniform Li-ion flux and reversible electrochemical reactions of the LMBs, effectively suppressing Li dendrite growth during cycling.

4 | Conclusion

In this study, we proposed PCELS integrating polymers, ceramic particles, and electrically conductive carbon for LMB separators to enhance the Li-ion conductivity and thereby achieve uniform Li-ion flux. The PCELS showed high electrolyte wettability on both its sides, facilitating rapid ion transport. Also, the ceramic particles and negatively charged polymers within the PCELS significantly improved the t_{Li^+} , enhancing Li-ion transport kinetics and uniformity of Li deposition. Moreover, the electrically conductive carbon within the PCELS provided additional electron transport channels and shortened ion transport pathways, significantly improving the charge-transfer kinetics and uniformity of Li-ion flux. With these effects acting synergistically, the PCELS showed significantly enhanced Li-ion conductivity, leading to excellent cycling stability in the Li metal half-cell tests, even at a high current density of 12.0 mA cm^{-2} . Also, the PCELS effectively suppressed Li dendrite growth during cycling, further demonstrating uniform Li-ion flux. Consequently, the PCELS showed excellent cycling stability in practical conditions of Li-S cells and Li|LFP full-cell tests. In conclusion, this study provides new insights

into the design of separators for LMBs and provides avenues for further studies toward the development of long-term stable LMBs.

Acknowledgements

This study was supported by the National R&D Program through the National Research Foundation of Korea (NRF), funded by the Ministry of Science and ICT (RS-2024-00408156 and RS-2024-00407282).

Conflicts of Interest

The authors declare no conflicts of interest.

References

1. B. Liu, J.-G. Zhang, and W. Xu, "Advancing Lithium Metal Batteries," *Joule* 2, no. 5 (2018): 833–845.
2. J. B. Goodenough and Y. Kim, "Challenges for Rechargeable Li Batteries," *Chemistry of Materials* 22, no. 3 (2010): 587–603.
3. S. Ferrari, M. Falco, A. B. Muñoz-García, et al., "Solid-State Post Li Metal Ion Batteries: A Sustainable Forthcoming Reality?", *Advanced Energy Materials* 11, no. 43 (2021): 2100785.
4. S. Chen, F. Dai, and M. Cai, "Opportunities and Challenges of High-Energy Lithium Metal Batteries for Electric Vehicle Applications," *ACS Energy Letters* 5, no. 10 (2020): 3140–3151.
5. W. Choi, M. Park, S. Woo, et al., "Towards Ultra-Stable and Dendrite-Suppressed Li-Metal Batteries: Ion-Regulating Graphene-Modified Separators," *Carbon* 230 (2024): 119576.
6. X. Zhang, L. Zou, Z. Cui, et al., "Stabilizing Ultrahigh-Nickel Layered Oxide Cathodes for High-Voltage Lithium Metal Batteries," *Materials Today* 44 (2021): 15–24.
7. H. Kim, S.-H. Lee, N.-Y. Park, J.-M. Kim, J.-Y. Hwang, and Y.-K. Sun, "Forming Robust and Highly Li-Ion Conductive Interfaces in High-Performance Lithium Metal Batteries Using Chloroethylene Carbonate Additive," *Advanced Energy and Sustainability Research* 5, no. 1 (2024): 2300151.
8. Z. Tong, C. Lv, G.-D. Bai, Z.-W. Yin, Y. Zhou, and J.-T. Li, "A Review on Applications and Challenges of Carbon Nanotubes in Lithium-Ion Battery," *Carbon Energy* 7, no. 2 (2025): e643.

9. J. Feng, C. Yang, L. Zhang, F. Lai, L. Du, and X. Yang, "First-Principle Calculation of Distorted T-Carbon as a Promising Anode for Li-Ion Batteries With Enhanced Capacity, Reversibility, and Ion Migration Properties," *Carbon Energy* 2, no. 4 (2020): 614–623.
10. Z. Li, C. Wang, X. Chen, et al., "MoO_x Nanoparticles Anchored on N-Doped Porous Carbon as Li-Ion Battery Electrode," *Chemical Engineering Journal* 381 (2020): 122588.
11. A. Yin, L. Yang, Z. Zhuang, et al., "A Novel Silicon Graphite Composite Material With Core-Shell Structure as an Anode for Lithium-Ion Batteries," *Energy Storage* 2, no. 4 (2020): e132.
12. M. Park, K. Lee, M. S. Kang, et al., "Crystallinity and Composition Engineering of Organic Crystal Derived 1D Carbons for Advanced Li-Metal Based Batteries," *Carbon* 233 (2025): 119870.
13. L. Chen, X. Fan, X. Ji, J. Chen, S. Hou, and C. Wang, "High-Energy Li Metal Battery With Lithiated Host," *Joule* 3, no. 3 (2019): 732–744.
14. Q. Li, S. Zhu, and Y. Lu, "3D Porous Cu Current Collector/Li-Metal Composite Anode for Stable Lithium-Metal Batteries," *Advanced Functional Materials* 27, no. 18 (2017): 1606422.
15. M. He, L. G. Hector, F. Dai, et al., "Industry Needs for Practical Lithium-Metal Battery Designs In Electric Vehicles," *Nature Energy* 9, no. 10 (2024): 1199–1205.
16. N. Zhu, Y. Yang, Y. Li, Y. Bai, J. Rong, and C. Wu, "Carbon-Based Interface Engineering and Architecture Design for High-Performance Lithium Metal Anodes," *Carbon Energy* 6, no. 1 (2024): e423.
17. X.-Q. Zhang, X.-B. Cheng, X. Chen, C. Yan, and Q. Zhang, "Fluoroethylene Carbonate Additives to Render Uniform Li Deposits in Lithium Metal Batteries," *Advanced Functional Materials* 27, no. 10 (2017): 1605989.
18. J. Wang, W. Huang, A. Pei, et al., "Improving Cyclability of Li Metal Batteries at Elevated Temperatures and Its Origin Revealed by Cryo-Electron Microscopy," *Nature Energy* 4, no. 8 (2019): 664–670.
19. P. Ma, Z. Zhuang, J. Cao, B. Ju, and X. Xi, "ZnO-CoO Composite Nanosphere Array-Modified Carbon Cloth for Low-Voltage Hysteresis Li Metal Anodes," *ACS Applied Energy Materials* 5, no. 5 (2022): 6417–6422.
20. J. Wang, B. Ge, H. Li, et al., "Challenges and Progresses of Lithium-Metal Batteries," *Chemical Engineering Journal* 420 (2021): 129739.
21. X. Fan, L. Chen, X. Ji, et al., "Highly Fluorinated Interphases Enable High-Voltage Li-Metal Batteries," *Chem* 4, no. 1 (2018): 174–185.
22. X. Shen, R. Zhang, P. Shi, X. Chen, and Q. Zhang, "How Does External Pressure Shape Li Dendrites in Li Metal Batteries?," *Advanced Energy Materials* 11, no. 10 (2021): 2003416.
23. Z. Zhuang, X. Rao, F. Zhang, V. V. Jadhav, and D. Q. Tan, "Plasma-Activated Tightly Bonded Uniform Metal-Organic Framework on Carbon Cloth for Stable Li Metal Anode," *Journal of Power Sources* 605 (2024): 234540.
24. V. V. Jadhav, Z. Zhuang, S. N. Banitaba, et al., "Tailoring the Performance of the LiNi_{0.8}Mn_{0.1}Co_{0.1}O₂ Cathode Using Al₂O₃ and MoO₃ Artificial Cathode Electrolyte Interphase (CEI) Layers Through Plasma-Enhanced Atomic Layer Deposition (PEALD) Coating," *Dalton Transactions* 52, no. 40 (2023): 14564–14572.
25. Z. Zhuang, C. Liu, Y. Yan, P. Ma, and D. Q. Tan, "Zn-C_xN_y Nanoparticle Arrays Derived From a Metal-Organic Framework for Ultralow-Voltage Hysteresis and Stable Li Metal Anodes," *Journal of Materials Chemistry A* 9, no. 47 (2021): 27095–27101.
26. D. Gandla, Z. Zhuang, V. V. Jadhav, and D. Q. Tan, "Lewis Acid Molten Salt Method for 2D Mxene Synthesis and Energy Storage Applications: A Review," *Energy Storage Materials* 63 (2023): 102977.
27. F. Wu, Y.-X. Yuan, X.-B. Cheng, et al., "Perspectives for Restraining Harsh Lithium Dendrite Growth: Towards Robust Lithium Metal Anodes," *Energy Storage Materials* 15 (2018): 148–170.
28. X.-R. Chen, B.-C. Zhao, C. Yan, and Q. Zhang, "Review on Li Deposition in Working Batteries: From Nucleation to Early Growth," *Advanced Materials* 33, no. 8 (2021): 2004128.
29. K. Yan, J. Wang, S. Zhao, et al., "Temperature-Dependent Nucleation and Growth of Dendrite-Free Lithium Metal Anodes," *Angewandte Chemie International Edition* 58, no. 33 (2019): 11364–11368.
30. X.-B. Cheng, C. Yan, H.-J. Peng, J.-Q. Huang, S.-T. Yang, and Q. Zhang, "Sulfurized Solid Electrolyte Interphases With a Rapid Li⁺ Diffusion on Dendrite-Free Li Metal Anodes," *Energy Storage Materials* 10 (2018): 199–205.
31. Z. Zhuang, F. Zhang, Y. Zhou, Y. Niu, Y. Yan, and D. Q. Tan, "Brittle Star-Like Nanoweb Modified Carbon Cloth Synthesized by Self-Templated Hollow Zeolitic Imidazolate framework-8 for Stable Li Metal Anodes," *Materials Today Energy* 30 (2022): 101192.
32. W. Tang, T. Zhao, K. Wang, et al., "Dendrite-Free Lithium Metal Batteries Enabled by Coordination Chemistry in Polymer-Ceramic Modified Separators," *Advanced Functional Materials* 34, no. 18 (2024): 2314045.
33. W. Ren, Y. Zheng, Z. Cui, Y. Tao, B. Li, and W. Wang, "Recent Progress of Functional Separators in Dendrite Inhibition for Lithium Metal Batteries," *Energy Storage Materials* 35 (2021): 157–168.
34. C. Wang, W. Li, Y. Jin, J. Liu, H. Wang, and Q. Zhang, "Functional Separator Enabled by Covalent Organic Frameworks for High-Performance Li Metal Batteries," *Small* 19, no. 28 (2023): 2300023.
35. Z. Zhuang, Y. Tang, B. Ju, and F. Tu, "In Situ Synthesis of Graphitic C₃N₄-poly(1,3-dioxolane) Composite Interlayers for Stable Lithium Metal Anodes," *Sustainable Energy & Fuels* 5, no. 9 (2021): 2433–2440.
36. Y. Yang, W. Wang, G. Meng, and J. Zhang, "Function-Directed Design of Battery Separators Based on Microporous Polyolefin Membranes," *Journal of Materials Chemistry A* 10, no. 27 (2022): 14137–14170.
37. Z. Zou, M. Yin, P. Yin, Z. Hu, D. Wang, and H. Pu, "Facile Preparation of Surface-Modified Polypropylene Nanofiber Separators With Enhanced Ionic Transport and Welding Performance for Lithium-Ion Batteries," *Nano Energy* 127 (2024): 109774.
38. H. Zheng, Y. Xie, H. Xiang, P. Shi, X. Liang, and W. Xu, "A Bifunctional Electrolyte Additive for Separator Wetting and Dendrite Suppression In Lithium Metal Batteries," *Electrochimica Acta* 270 (2018): 62–69.
39. Y. Ji, C. Yang, J. Han, and W. He, "Functional Separators for Modulating Li-Ion Flux Toward Uniform Li Deposition: A Review," *Advanced Energy Materials* 14, no. 38 (2024): 2402329.
40. X. Mao, L. Shi, H. Zhang, et al., "Polyethylene Separator Activated by Hybrid Coating Improving Li⁺ Ion Transference Number and Ionic Conductivity for Li-Metal Battery," *Journal of Power Sources* 342 (2017): 816–824.
41. Y. Zhao, J. Yan, J. Yu, and B. Ding, "Advances in Nanofibrous Materials for Stable Lithium-Metal Anodes," *ACS Nano* 16, no. 11 (2022): 17891–17910.
42. Z. Zhuang, B. Ju, P. Ma, L. Yang, and F. Tu, "Ultrathin Graphitic C₃N₄ Lithiophilic Nanosheets Regulating Li⁺ Flux for Lithium Metal Batteries," *Ionics* 27, no. 3 (2021): 1069–1079.
43. W. Zhang, Z. Tu, J. Qian, S. Choudhury, L. A. Archer, and Y. Lu, "Design Principles of Functional Polymer Separators for High-Energy, Metal-Based Batteries," *Small* 14, no. 11 (2018): 1703001.
44. Y. Wang, K. Zhou, L. Cui, et al., "Ion Transport Regulation of Polyimide Separator for Safe and Durable Li-Metal Battery," *Journal of Power Sources* 591 (2024): 233853.
45. J. Park, Y. J. Kwon, J. Yun, et al., "Ultra-Thin SiO₂ Nanoparticle Layered Separators by a Surface Multi-Functionalization Strategy for Li-Metal Batteries: Highly Enhanced Li-Dendrite Resistance and Thermal Properties," *Energy Storage Materials* 65 (2024): 103135.

46. W. Raza, A. Mehmood, A. Hussain, et al., "Designing Dendrite Resistive Poly (Ether-Ether-Ketone) Modified Multifunctional Celgard Separator for Lithium Metal Batteries: Mechanistic and Experimental Study," *Journal of Energy Storage* 90 (2024): 111717.
47. J. Wang, Y. He, Q. Wu, et al., "A Facile Non-Solvent Induced Phase Separation Process for Preparation of Highly Porous Polybenzimidazole Separator for Lithium Metal Battery Application," *Scientific Reports* 9, no. 1 (2019): 19320.
48. X. Zhang, F. Ma, K. Srinivas, et al., " Fe_3N @N-doped Graphene as a Lithiophilic Interlayer for Highly Stable Lithium Metal Batteries," *Energy Storage Materials* 45 (2022): 656–666.
49. S. Yang, J. Kim, S. Lee, J. Seo, J. Choi, and P. J. Kim, "Uniform Li Deposition Through the Graphene-Based Ion-Flux Regulator for High-Rate Li Metal Batteries," *ACS Applied Materials & Interfaces* 16, no. 3 (2024): 3416–3426.
50. Z. Zhuang, L. Yang, B. Ju, et al., "Ameliorating Interfacial Issues of $\text{LiNi}_{0.5}\text{Co}_{0.2}\text{Mn}_{0.3}\text{O}_2$ /Poly(propylene Carbonate) by Introducing Graphene Interlayer for All-Solid-State Lithium Batteries," *ChemistrySelect* 5, no. 7 (2020): 2291–2299.
51. Z. Zhuang, L. Yang, B. Ju, et al., "Engineering $\text{LiNi}_{0.5}\text{Co}_{0.2}\text{Mn}_{0.3}\text{O}_2$ /poly(propylene Carbonate) Interface by Graphene Oxide Modification for All-Solid-State Lithium Batteries," *Energy Storage* 2, no. 2 (2020): e109.
52. G. Kresse and J. Furthmüller, "Efficient Iterative Schemes for Ab Initio Total-Energy Calculations Using a Plane-Wave Basis Set," *Physical Review B* 54, no. 16 (1996): 11169–11186.
53. P. E. Blöchl, "Projector Augmented-Wave Method," *Physical Review B* 50, no. 24 (1994): 17953–17979.
54. J. P. Perdew, K. Burke, and M. Ernzerhof, "Generalized Gradient Approximation Made Simple," *Physical Review Letters* 77, no. 18 (1996): 3865–3868.
55. X. Hou, L. Li, S. Wei, J. Li, and F. Wu, "Two-Dimension Al_2O_3 -AlN Heterogeneous Nanosheets as Bifunctional Host Materials for Kinetics-Accelerated and Dendrite-Free Lithium-Sulfur Batteries," *Electrochimica Acta* 464 (2023): 142887.
56. J. Holtmann, M. Schäfer, A. Niemöller, M. Winter, A. Lex-Balducci, and S. Obeidi, "Boehmite-Based Ceramic Separator for Lithium-Ion Batteries," *Journal of Applied Electrochemistry* 46, no. 1 (2016): 69–76.
57. Z. Hao, C. Wang, Y. Wu, et al., "Electronegative Nanochannels Accelerating Lithium-Ion Transport for Enabling Highly Stable and High-Rate Lithium Metal Anodes," *Advanced Energy Materials* 13, no. 28 (2023): 2204007.
58. M. Park, S. Woo, J. Seo, J. Choi, E. Jeong, and P. J. Kim, "Directing the Uniform and Dense Li Deposition Via Graphene-Enhanced Separators for High-Stability Li Metal Batteries," *Electrochimica Acta* 495 (2024): 144426.
59. X. Wang, R. Huang, S. Niu, et al., "Research Progress on Graphene-Based Materials for High-Performance Lithium-Metal Batteries," *New Carbon Materials* 36, no. 4 (2021): 711–728.
60. A. Ghorbani-Choghamarani, H. Aghavandi, and M. Mohammadi, " $\text{Boehmite@SiO}_2@\text{Tris}(\text{Hydroxymethyl})\text{Aminomethane-Cu(I)}$: A Novel, Highly Efficient and Reusable Nanocatalyst for the C-C Bond Formation and the Synthesis of 5-Substituted 1H-tetrazoles in Green Media," *Applied Organometallic Chemistry* 34, no. 10 (2020): e5804.
61. G. Surekha, K. V. Krishnaiah, N. Ravi, and R. Padma Suvarna, "FTIR, Raman and XRD Analysis of Graphene Oxide Films Prepared by Modified Hummers Method," *Journal of Physics: Conference Series* 1495, no. 1 (2020): 012012.
62. X. Wang, W. Zeng, L. Hong, et al., "Stress-Driven Lithium Dendrite Growth Mechanism and Dendrite Mitigation by Electroplating on Soft Substrates," *Nature Energy* 3, no. 3 (2018): 227–235.
63. S. Kalnaus, Y. Wang, and J. A. Turner, "Mechanical Behavior and Failure Mechanisms of Li-Ion Battery Separators," *Journal of Power Sources* 348 (2017): 255–263.
64. S. H. Yoo and C. K. Kim, "Enhancement of the Meltdown Temperature of a Lithium Ion Battery Separator via a Nanocomposite Coating," *Industrial & Engineering Chemistry Research* 48, no. 22 (2009): 9936–9941.
65. D. Han, X. Wang, Y.-N. Zhou, et al., "A Graphene-Coated Thermal Conductive Separator to Eliminate the Dendrite-Induced Local Hot-spots for Stable Lithium Cycling," *Advanced Energy Materials* 12, no. 25 (2022): 2201190.
66. X. Zhou, X. Li, Z. Li, et al., "Hybrid Electrolytes With an Ultrahigh Li-Ion Transference Number for Lithium-Metal Batteries With Fast and Stable Charge/Discharge Capability," *Journal of Materials Chemistry A* 9, no. 34 (2021): 18239–18246.
67. C.-E. Lin, H. Zhang, Y.-Z. Song, Y. Zhang, J.-J. Yuan, and B.-K. Zhu, "Carboxylated Polyimide Separator With Excellent Lithium Ion Transport Properties for a High-Power Density Lithium-Ion Battery," *Journal of Materials Chemistry A* 6, no. 3 (2018): 991–998.
68. J. N. Chazalviel, "Electrochemical Aspects of the Generation of Ramified Metallic Electrodeposits," *Physical Review A* 42, no. 12 (1990): 7355–7367.
69. P. Bai, J. Li, F. R. Brushett, and M. Z. Bazant, "Transition of Lithium Growth Mechanisms in Liquid Electrolytes," *Energy & Environmental Science* 9, no. 10 (2016): 3221–3229.
70. J. Evans, C. A. Vincent, and P. G. Bruce, "Electrochemical Measurement of Transference Numbers in Polymer Electrolytes," *Polymer* 28, no. 13 (1987): 2324–2328.
71. G. Zhang, P. Li, K. Chen, et al., "A Robust Janus Bilayer With Tailored Ionic Conductivity and Interface Stability for Stable Li Metal Anodes," *Journal of Energy Chemistry* 74 (2022): 368–375.
72. C. Zhu, T. Nagaiishi, J. Shi, et al., "Enhanced Wettability and Thermal Stability of a Novel Polyethylene Terephthalate-Based Poly(Vinylidene Fluoride) Nanofiber Hybrid Membrane for the Separator of Lithium-Ion Batteries," *ACS Applied Materials & Interfaces* 9, no. 31 (2017): 26400–26406.
73. M. M. U. Din and R. Murugan, "Metal Coated Polypropylene Separator With Enhanced Surface Wettability for High Capacity Lithium Metal Batteries," *Scientific Reports* 9, no. 1 (2019): 16795.
74. J. Kim, S. Park, S. Hwang, and W.-S. Yoon, "Principles and Applications of Galvanostatic Intermittent Titration Technique for Lithium-Ion Batteries," *Journal of Electrochemical Science and Technology* 13, no. 1 (2022): 19–31.
75. D. W. Dees, S. Kawauchi, D. P. Abraham, and J. Prakash, "Analysis of the Galvanostatic Intermittent Titration Technique (GITT) as Applied to a Lithium-Ion Porous Electrode," *Journal of Power Sources* 189, no. 1 (2009): 263–268.
76. Z. Zhuang, F. Zhang, D. Gandla, et al., "Metal–Organic Framework-Derived ZnO_xN Dually Doped Nanocages as an Efficient Host for Stable Li Metal Anodes," *ACS Applied Materials & Interfaces* 15, no. 32 (2023): 38530–38539.
77. J. Zhou, S. Sun, X. Zhou, et al., "Defect Engineering Enables an Advanced Separator Modification for High-Performance Lithium-Sulfur Batteries," *Chemical Engineering Journal* 487 (2024): 150574.
78. X. Liang, X. Li, Q. Xiang, et al., "Surficial Oxidation of Phosphorus for Strengthening Interface Interaction and Enhancing Lithium-Storage Performance," *Nano Letters* 22, no. 23 (2022): 9335–9342.
79. F. Zeng, Z. Jin, K. Yuan, et al., "High Performance Lithium-Sulfur Batteries With a Permselective Sulfonated Acetylene Black Modified Separator," *Journal of Materials Chemistry A* 4, no. 31 (2016): 12319–12327.

Supporting Information

Additional supporting information can be found online in the Supporting Information section.